Investigations on micro-mechanical properties of polycrystalline Ti(C,N) and Zr(C,N) coatings

Idriss El Azhari[a,b], José Garcia[c,*], Mohammad Zamanzade[d], Flavio Soldera[a], Christoph Pauly[a], Luis Llanes[b], Frank Mücklich[a]

[a] Functional Materials, Department of Materials Science and Engineering, Saarland University, Campus D 3.3, D-66123 Saarbrücken, Germany

[b] Materials Science and Metallurgical Department (CIEFMA), Barcelona School of Engineering (EEBE), Universitat Politècnica de Catalunya, 08019, Barcelona, Spain

[c] Sandvik Coromant R&D, SE-126 80, Stockholm, Sweden

[d] Materials Science and Methods, Department of Materials Science and Engineering, Saarland University, Campus D 2.2, D-66123 Saarbrücken, Germany

*Corresponding author: jose.garcia@sandvik.com

Abstract

Hard and wear resistant coatings are widely used as tribological layers to protect tools from wear, oxidation and corrosion. Characterizing the deformation behavior of coatings is essential for understanding wear mechanisms and to design multi-layered coatings that withstand severe working conditions. Micro-mechanical properties of Ti(C,N) and Zr(C,N) coatings deposited by chemical vapor deposition on a WC-Co cemented carbide substrate were examined by micro-compression testing using a nanoindenter equipped with a flat punch. Scanning Electron Microscopy, Focused Ion Beam, Electron Backscattered Diffraction and Finite Element Modeling were combined to analyze the deformation mechanisms of the carbonitride layers at room temperature. The results revealed that Ti(C,N) undergoes

a pure intergranular crack propagation and grain decohesion under uniaxial compression; whereas the fracture mode of Zr(C,N) was observed to be inter/transgranular failure with unexpected plastic deformation at room temperature.

Keywords

CVD coatings, Micro-compression, Plasticity, Zr(C,N), Ti(C,N), Finite Element Modeling, EBSD.

1. Introduction

The increase of production efficiency in metal cutting industry is vital for the reduction of manufacturing costs. This can be achieved by developing coated cemented carbide systems that can withstand high cutting speeds and severe service conditions. Hence, the strategy is to focus not only on the design of new cemented carbide substrate, but also on the design of thin hard films with optimized properties by tailoring their composition, texture and particle size among others [1]. Moreover, both high hardness and adequate toughness are essential for the thin layers and their combination with the cemented carbide substrate [2], given that high hardness come at the expense of toughness and vice versa [3].

The present study deals with micro-mechanical investigations of transition metal Zirconium and Titanium carbonitrides (Zr(C,N) and Ti(C,N) respectively) coatings deposited by chemical vapor deposition (CVD) on WC-Co cemented carbide. They both have good combination of high hardness and adequate toughness [4] and comparable physical properties [5,6]. However, they present different performances during metal cutting applications [7]. Then, in order to understand this different wear behavior, it is of great importance to investigate their deformation mechanisms at the micro-scale, such that micro-mechanical response may be correlated to microstructure features.

Studies on single crystalline and sintered transition-metal carbides (TMC) flourished between 60s and 80s due to historical reasons [8]. The focus was on studying the mechanical properties and plasticity at high temperature of these compounds [9–18] because of their outstanding potential in extreme

environment such as aerospace applications and metal cutting. From late 90s on, as it was understood that different hybrid properties (ceramic and metal-like) in these materials originated from their electronic structures and atomic bonding, and with the boost of computing capabilities, extensive fundamental research based on the first principles calculations has been conducted to explain their mechanical and physical properties [19–29]. In general, it is agreed that the TMC are ductile at high temperatures, yet they are brittle at room temperature and fail through cracking because of limited or absence of dislocation activity. Recently, Kiani et al. have proven through Transmission Electron Microscopy in-situ compression of ZrC single crystals that they deform, indeed, plastically at room temperature through dislocation motion along two active slip systems [27].

Nanoindentation is the standard and most frequent method used to characterize mechanical properties of thin film materials [30]. Accordingly, studies on deformation mechanisms of thin films variants of transition-metals carbides/nitrides (TMC/N) were mainly performed through micro/nano-indentation experiments combined with modeling [31–36]. Intergranular shear sliding is identified as a common and important failure mechanism in these studies. Nevertheless, investigation of the deformation mechanisms from the residual imprints is not always easy because of the multi-axial stress-strain created during indentation [37–41]. Micro-compression test has shown to be a more adaptable method to investigate the micro-mechanics on a small defined geometry [42], and it has the advantage - over nanoindentation - of a relatively more uniform stress-strain field [41]. This testing technique has gained increased interest in the recent years to acquire knowledge on the micromechanics that govern deformation mechanisms in different classes of materials [40,42,43], including brittle materials as the biggest challenge of premature failure during testing is circumvented by the miniaturization of the tested size [44]. However, this technique is fundamentally used to characterize single crystalline materials. Analogous studies for hard coatings are scarce, and to the best knowledge of the authors, micro-compression investigations of polycrystalline hard coatings are limited to few studies [30,45–50], and for transition metal carbonitrides are rather missing.

In order to fill the missing gap of the current knowledge in terms of deformation mechanics of TMCN, we present and compare results on deformation of hard coatings (Ti(C,N) and Zr(C,N)) during micro-

compression. The target is to reveal which are the microstructural features that controls the mechanical properties and deformation behavior in polycrystalline coatings produced in industrial CVD reactor. The study is mainly composed of two sections. The first one presents the general results and basic observations, which are the starting point for the upcoming discussions. In the second section, the influence of the adopted experimental protocol on the results is reviewed based on Finite Element Modeling (FEM) and other investigations. Then, the deformation mechanism of each carbonitride coating is presented based on Scanning Electron Microscope (SEM) and Electron Backscattered Diffraction (EBSD) results.

2. Experimental

2.1. Coating deposition

Each Ti($C_{0.5}$,$N_{0.5}$) and Zr($C_{0.5}$,$N_{0.5}$) coating was deposited on a WC-6wt%Co substrate at around 900 ℃ in a hot wall CVD reactor using $TiCl_4$, $ZrCl_4$ and CH_3CN as gas precursors. The final thickness of the coating was 5 µm. A thin TiN layer of 0.3 µm was previously deposited on the cemented carbide to enhance the adherence of the carbonitride coating and hinder reactions and diffusion with the substrate. (See Figure 1). Mechanical properties of the materials taken from literature are shown in Table 1.

2.2. Pillar milling

Because a flat and roughness free surface is required for pillars fabrication, the surface topography inherited from the coating growth process was gently smoothed by a stepwise polishing up to 1 µm. To avoid damaging the coating and limit the residual stress changes - which could be inflicted during polishing - low rotation speed and force were applied with the use of a diamond suspension (ranging from 9 µm to 1 µm) sprayed on polishing cloth. The sample was mounted in a FEI Helios Nanolab Dualbeam 600 SEM/FIB that operates with gallium (Ga) ion beam. To achieve the final shape of the pillar three annular milling steps are used with a current decreasing from 21 nA, 0,92 nA to 0,28 nA. Many challenges were faced during the milling as the following scope statement must be respected for reproducible experiments: (a) A standard aspect ratio of 1/3 (diameter/height) should be maintained [51].

(b) The pillar must be based and emerging from the coating (i.e. direct contact with the substrate must be avoided) to reduce as much as possible the substrate compliance and response during compression (Figure 1 (a), (b)). Because of the latter condition, the pillars have a relatively higher tapering angle varying from 4° to 6° since an additional fine-mill ing step to reduce the tapering would mill the whole layer and reach the cemented carbide substrate. Subsequently, the final pillar diameter ranges from 1 µm to 1.1 µm and the length from 3 µm to 3.4 µm. Our effort came up short to suppress the irregularities at the pillar base, as it is an intrinsic property of the coating itself related to the orientation of the grains that influences the material removal rate (Figure 1 (c)).

Figure 1:

2.3. Compression test

Compression tests were performed with the aid of a Hysitron Tribo-Indenter TI 900, equipped with a Performech controller and a 5 µm diamond flat punch. The loading function is a displacement controlled with a constant rate of 3 nm/s and a maximum depth of 120 nm. Twelve pillars were tested for each coating following the same experimental strategy.

After the compression test, inspection was conducted with Scanning Electron Microscopy (SEM). The irregularities around the pillar and the non-flat base surface make the determination of the actual pillar height very difficult. Hence, the numerical estimation of engineering strain was not possible to determine with a simple equation and requires rather Finite Element Modeling (FEM) for each case. As mentioned above, further fine milling could suppress easily both the tapering and irregularities; nevertheless, the pillar would be based on the substrate and the assessment of the pillar's referred base (for strain calculation) will remain still not accessible, as the pillar would be in this case partly submerged in the substrate.

Therefore, the engineering stress (quotient of applied force and the top area of the pillar) versus displacement are the chosen parameters for the representation of the curves. We note that the raw data is plotted without fitting or smoothing the curves.

2.4. Finite Element Analysis (FEM)

A 3D finite element analysis with ANSYS APDL was done to have an overview of the stress distribution, the elastic deformation and the interaction between the pillar, coating, bonding layer and the substrate during the compression test. The polycrystallinity of the coatings and multiple phases in the substrate phases were reduced to an isotropic and homogeneous condition for each material. The different properties of the coatings were taken from reference [6] and for the substrate from the Sandvik Coromant R&D database (Table 1). A displacement controlled loading function was simulated.

Table 1: Mechanical properties of different materials (* [6]; ** Sandvik Coromant database) .

Material	**Young´s modulus E (GPa)**	**Shear modulus G (GPa)**
$Zr(C_{0,5},N_{0,5})$*	405	172
$Ti(C_{0,5},N_{0,5})$*	463	194
TiN*	465	189
WC-Co**	626	257

2.5. Electron Backscattered Diffraction (EBSD) characterization

Analysis of compressed pillars (in terms of cracking, microstructure and deformation) was conducted on a lamella taken from the pillar and prepared with a procedure similar to the one used for preparation of Transmission Electron Microscopy (TEM) samples. First, the pillar was covered by Platinum (Pt) which was deposited with Electron Beam Induced Deposition (EBID) and subsequently with Ion Beam Induced Deposition (IBID). In this way, the surface of the pillars was not damaged when working with ions for

cutting and transferring the lamella and sharp edges could be maintained during the final polishing with ions. This lamella was milled at the pillar center with Focused Ion Beam (FIB), lifted out with an OMNIPROBE manipulator and deposited on a TEM grid holder for final polishing on a single side only, leaving the sample rather thick (about 500 nm) since electron transparency is not required. Finally, EBSD was conducted in reflection mode with an EDAX Hikari system. As the EBSD surface is very sensitive to surface condition [52], low current and acceleration (11 pA and 5-2 kV respectively) voltage was used during the final polishing of the lamella in order to minimize any possible damage with Ga^+ ions.

Diffraction patterns were obtained in reflection mode at 20 kv acceleration voltage, 11 nA current and a 20 nm step size. Subsequently the raw data was processed and analyzed with OIM 7^{TM} Data Analysis software. The processing consists of defining a grain as an island of at least five adjacent points with a maximum misorientation of 5 degrees. Afterwards the confidence index (CI) was standardized across each grain and finally noise and poor data were filtered by a cut-off of CI=0.09. No morphological operation (e.g. dilation operation) was used to enhance the representability of the EBSD maps.

The choice of EBSD for orientation imaging comes from the fact that it has a series of advantages over conventional TEM (i.e. using the spot diffraction patterns), among others being faster, automated for mapping, easier and with higher angular accuracy [53]. Moreover, it provides additional information about the long range and short range misorientation character like Kernel Average Misorientation (KAM) [54] and is more adapted for studying polycrystalline materials (Since for TEM, the sample has to be tilted according to the zone axis of each grain).

3. Results and discussion

3.1. Stress-Displacement curves

3.1.1. Ti(C,N) coating

The deformation of pillars starts with a linear regime followed by pop-ins (or strain bursts), afterwards catastrophic failure occurs immediately (see Figure 2 (a)). Indeed, if we consider that the pop-in load

state as the yield strength, then a high yield strength of 14 GPa was reached which is comparable to some of the highest yield values reported on compression tests of hard materials: CrAlN/Si_3N_4 (16 GPa) [47], ZrB_2 (13.4 GPa) [55], GaN (7.8 GPa) [56] and WC (6.6 GPa) [57]. No clear deformation insight could be extracted after complete destruction of the pillar apart from the fact that the debris have the shape of the initial columnar grains (see Figure 2 (b)). Thus, to preserve the pillar integrity after the compression test and to unveil the origin of pop-ins, the flat punch was quickly unloaded after the appearance of a pop-in in the stress-displacement curve.

Figure 2:

Subsequently, using this method has enabled, on the one hand, the observation of the deformation inflicted on pillars and, on the other hand, to correlate the observed event in the curves to the changes of the pillars. Figure 3 shows intergranular crack formation at the circumference of the pillar after appearance of the pop-in.

Figure 3:

3.1.2. Zr(C,N) coating

For the Zr(C,N) coatings the curves look in general similar to Ti(C,N); the curves start with linear behavior followed by a pop-in. Thereafter, if the experiment is not terminated, a catastrophic failure will take place. However, two major differences compared to the behavior of Ti(C,N) coatings were noticed: (a) The stiffness of Ti(C,N) coating is higher than the Zr(C,N). (b) The cracking related to the pop-ins is different, in comparison to Ti(C,N), which is generally partial cracking on the top surface following an undefined pattern giving the impression of a mixed inter/intragranular propagation behavior (see Figure 4 (b) and (c)).

Figure 4:

Figure 5 (a) (which presents a summary of all the curves for both coatings) indicates that stress-displacement curves are reproducible and similar with a leaning for each coating. The ultimate strength

is similar among most of the curves, however, the pop-ins occur at higher displacements for Zr(C,N) which is an indication of superior toughness compared with Ti(C,N). The small disparities within each coating family are more related to the variations of tapering angle from one pillar to another, which affects the stiffness directly. H. Fei et al. [41] have shown that if the tapering angle is lower than 5°, then its effect is negligible on the stress. The same tendency can be recognized in Figure 5 (b) where the slope of stress-displacement curves were plotted against the tapering angle of each pillar. We observe that when the tapering angle is higher than 5° the disparities between the points increase.

Figure 5:

3.2. Influence of the substrate during compression

Depending on the experimental setup, the base substrate below the coating can have a major impact during compression. Thereby, the deformation mechanisms of the pillar coating can be influenced and the stiffness will be affected [46] . In the present study, sink-in of the pillar during compression is reduced by higher taper angle [41]. Indeed, the deformation could be probed also from the substrate instead. On the one hand, the topography of the substrate at the micrometric scale is wavy and we could have a pillar based directly or very close to the substrate even if the pillar's base is not showing any trace of it. On the other hand, the local properties of the cemented carbide may not be uniform owing to a randomly distributed WC grains in a cobalt matrix [58]. To investigate these effects, serial cross sections with the FIB were conducted for a destroyed pillar, which has been stressed up to 14 GPa (Figure 6 (a)). The cross section in Figure 6 (b) shows that 1 µm coating (including the TiN bonding layer) separates the pillar from the substrate and no damage was detected in the vicinity of the supporting coating even with the diamond flat punch crushing of the debris against the supporting coating during catastrophic failure. This result is in a good agreement with finite element modeling. We can see in Figure 7 that the major displacement/deformation is localized and maximum at the pillar top part, and it is compressive following a gradient along the Y axis. More importantly in this discussion, the displacement is confined within the carbo-nitride coating, which is in consistency with our experimental setup. Thereby, considering these

results, cracking of the supporting interlayer (between the substrate and the coating) during pillar´s compression is discarded.

Figure 6:

Figure 7:

In case the pillar is sitting directly on very soft spot on the substrate (formed mainly by cobalt), the pillar acts as an extension of the flat punch and consequently the substrate is indented/probed first because it is softer than the coating, then at a certain stress state the coating starts to deform. This assumption is proven in comparing the curves of a compliant WC-Co substrate pillar, a Ti(C,N) pillar settling on a similar WC-Co substrate and a normal pillar (Figure 8). We notice clearly that the first half of the red curve (corresponding to the coating pillar based on the substrate) overlaps the substrate curve (green curve), then at a higher stress the slope of the red curve become more regular and similar to the normal pillar curve (blue). In short, this means that in case of a pillar located near a softer substrate spot, we will see a non-linear stress-displacement curve during the early stages, and then this result will be discarded.

Figure 8:

3.3. Deformation mechanisms

The discussion of results must consider that the pillar compression is performed on polycrystalline material with a variety of grain sizes including small and bigger crystals, which means that every pillar has different distribution of grain size, crystal orientations and defects (CVD cooling cracks). This fact makes each pillar respond relatively different toward the applied load. Besides, it has been reported that

the scattering of the results increases as the size of the pillar approaches the microstructural dimensions [30,45,59].

3.3.1. Deformation mechanisms of Ti(C,N)

For Ti(C,N) an elastic deformation was first observed, followed by the pop-in which corresponds to crack initiation between the grains (Figure 2). It is then suggested that the failure takes place according to purely columnar grain dissociation or intercolumnar cracking.

Yong et al. [35], performed nano-indentation with a spherical diamond indenter to investigate the failure modes of Ti(C,N) coating. They also stated inter-columnar cracking along the grain boundary as the first failure event, which took place as the indentation load increased. The location of these cracks within the Ti(C,N) layer corresponded to the highest calculated strain energy density with FEM. Calculating the same parameter in our FEM model in Figure 9, we find out that that inter-columnar cracking occurred at the apex part where also maximum strain energy density was calculated.

Figure 9:

Similar columnar grain decohesion during pillar compression has been reported by Yu Zou et al. [45] for Nb-Mo-Ta-W high entropy alloys (HEA) having similar characteristics (polycrystalline, columnar structured, generally brittle at room-temperature and high yield strength). They noticed that pillars having a diameter more than 1 µm experienced cracking at the top and cracks propagate along the grain boundaries showing intergranular fracture. They draw an analogy to bundled bamboos to describe the structure of the columnar grains inside the pillar, and suggested that it is like if the compression was performed on a discrete array of single-crystalline pillars, and if the deformation in each grain cannot be accommodated by its neighbors, it may lead to crack initiation along the grain boundaries [45]. The reason behind this mechanism could be attributed to the low cohesive strength at the grain boundaries of this HEA alloy [45,60,61].

In Figure 10, an example that endorses strongly this assumption is shown. The post-compression SEM images of Ti(C,N) pillars shows an evident decohesion of the grains and cracks follows perfectly the intergranular pattern. This extended decohesion is translated by a non-linear stress-displacement curve after elastic part (Figure 10 (c)). Furthermore, topography/steps on the pillar top surface is spotted which is probably attributed either to the grain sliding or to the elastic recovery (after unloading) that became specific to each grain orientation after dissociation.

Figure 10

Summarizing the deformation mechanism of the Ti(C,N) pillar can be resumed as following: in the beginning the polycrystalline Ti(C,N) pillar deforms elastically toward the applied load as one structure. As the deformation continues, the stress is accumulating at the grain boundaries as they are the weak spots in the structure and also because each crystal has a specific stiffness (according to its orientation). When higher stresses are reached, the grains begin to slide along the grain boundaries. Then, at a given critical load, cracks will initiate at the top face of the pillar as a result of maximum strain energy in this region, then they will propagate along the columnar grain boundaries which causes grain decohesion and finally catastrophic failure (Figure 2 (b)).

3.3.2. Deformation mechanisms of Zr(C,N)

The fracture images of the Zr(C,N) pillar showed that the crack pattern is different compared to the Ti(C,N) pillar (discontinuous partial cracking and undefined pattern (Figure 4)). It can be assumed that the crack propagation shows a rather random pattern and mixed mode (inter/intragranular). In addition, no decohesion and no steps (on the top face) between the grains were seen, and the cracks were fine and difficult to observe (in some cases) which may indicate a high cohesive strength between the grains. Nevertheless, two important facts were noticed during the compression of Zr(C,N) compared to Ti(C,N). First, few pillars did-not show pop-ins even at stresses exceeding 12 GPa. SEM examination of the pillars after compression test did not reveal any structural changes in the pillars. This led us to retest

these resistant pillars until a pop-in took place. Surprisingly, when comparing the curves of the 1st and 2nd compression (Figure 11) the outcome was a strain hardening behavior like the one observed in metals. This may be considered as a clear indication of a plastic deformation for Zr(C,N) pillars. The second fact was that in one Zr(C,N) pillar endured material extrusion at the top ring and buckling was also recognized at the same side (Figure 12 (a)). To investigate the deformation mechanism, a cross section was performed at the middle of the pillar and interestingly buckling was noticed at the right side (Figure 12 (b)). Afterwards, a lamella was extracted from this pillar to observe closely the inner microstructure with EBSD (Figure 12 (c)). Similar procedure was done for a deformed Ti(C,N) pillar (Figure 12 (d-f)) and both results are compared and discussed in the following section.

Figure 11:

Figure 12:

3.4. EBSD analysis

3.4.1. Inverse pole figure (IPF)

Figure 12 (c) and (f) presents the IPF map of Zr(C,N) and Ti(C,N) pillars after the compression tests respectively. Polycrystallinity, randomness of the texture and the columnar microstructure of the pillars are visible. The Zr(C,N) has a buckled shape compared to Ti(C,N) especially at the right side where we can see that the obvious buckling (Figure 12 (b)) is coming from a single elongated grain.

3.4.2. Schmidt factor

The Schmidt factor was calculated (Figure 13) individually for each grain considering a perpendicular compression and presumably one active slip system: $\{001\}\langle 110\rangle$ for Zr(C,N) [11,27] and $\{110\}\langle 1\bar{1}0\rangle$ for Ti(C,N) [14,28]. Due to the scarcity of data in carbonitride systems and the similar properties between carbides and carbonitrides, this data was taken from ZrC and TiC respectively. We would like to emphasize here that for ZrC, Schmidt factors were calculated by considering only one slip system as, on

the one hand, it is the favorable one due to easy shear in comparison to $\{110\}\langle 1\bar{1}0\rangle$ [27] and, on the other hand, we wanted to test minimal conditions to expect activation of slip systems in ZrC grains.

High Schmidt factor means that either the proper orientation (before compression) was favorable for plastic deformation or that it is a result of a crystal rotation. For Zr(C,N), interestingly, maximum Schmidt factor is observed at the grain where material extrusion originated from, and the buckled grain (at the right side of the pillar) exhibits a gradient of the Schmidt factor (Figure 13 (a)). Moreover, by comparing the distributions in Figure 13 (d), we can discern a higher and sharp Schmidt factor distribution for Zr(C,N) shifted to high values that are close to the maximum theoretical value of 0.5. In other words, in contrast to Ti(C,N) (Figure 13 (b)) where random values are spread over the map and the corresponding distribution is spread, Zr(C,N) grains with high Schmidt factor corresponds to the areas where deformation was observed. These observations are an indication that higher Schmidt factors are not only related to the initial state, but also as a result of grain rotation. Arguably, in our experiments the pillar (as one structure) would in extreme conditions experience a maximum strain of 3.3% and it is far from causing such grain rotation effect. However, again we draw the attention that, on the one hand, the pillar has tapered geometry, which results in a concentration of most displacement at the upper part. On the other hand, the pillar is composed of polycrystalline grains, which are depending on the orientation, grain size, contiguity to other grains and location in the pillar, are more or less prone to deform. Accordingly, to have a better insight, the calculation of a misorientation parameter will be of relevance.

Figure 13:

3.4.3

. Misorientation analysis

Misorientation is considered to be an indication of strain distribution in the material [62]. Besides, earlier studies on FCC materials have shown that the increase of misorientation is linearly related to the square root of the strain ($\theta \propto \sqrt{\varepsilon}$) during cold deformation [54,63,64], and it was experimentally proven that when the strain increases, the misorientation distribution is shifted toward higher angles and the angular spread increases as well [54,63,65].

In Figure 14, misorientation mapping is used to calculate the misorientation of each pixel within a grain with respect to a user defined reference point (selected at the bottom of each grain). This parameter was calculated for both Ti(C,N) and Zr(C,N) and has given a strong confirmation of the postulated presumptions.

A clear misorientation gradient is visible along the loading vertical axis for Zr(C,N) grains, not only on particular regions but rather on the entire pillar structure. Actually, this misorientation tendency is not related to the deposited state but rather to the deformation, since firstly, the observed vertical gradient cannot be produced by thermal residual stresses, which are acting horizontally; and secondly, residual stresses are relaxed gradually during successive annular milling of the pillar [66,67] and during the lamella preparation [68]. Therefore, the observed gradient means that not only some grains underwent a deformation, yet every component had absorbed the strain energy plastically. However, as discussed before, some grains are more prone to deform than others. To highlight the strong gradient in misorientation, a line is sketched to calculate the profile vector on each map and the result is presented in Figure 14 (c) where we can see quantitatively the strong gradient within Zr(C,N) grains. Similar deformation gradient was observed in the FEM model of strain energy density (Figure 9).

The occurrence of gradients is a sign that the grains have undergone a partial rotation to accommodate the strain energy. In a study about the development of gradient orientations at different grain scales Gurao et al. [69] confirmed that in microcrystalline FCC grains, plastic deformation is carried by crystallographic slip that contributes to evolution of orientation gradients through the formation of Grain Boundary Affected Zone (GBAZ) that takes over a major fraction of the entire grain [69]. Same observation is valid for Zr(C,N) grains in the pillar investigated, knowing that Zr(C,N) is an FCC rock salt structure where C and N atoms occupy interstitial octahedral sites [70], and generally transition metal carbides deform on slip systems analogous to FCC metals [71]. Particularly, it was reported that the mechanical response of ZrC in compression is similar to FCC metals rather than a B1 structured ionic compound [27].

Another misorientation parameter called Kernel Average Misorientation (KAM) was calculated. It has been shown that the latter is correlated to the deformation microstructure and can be used to study the

evolution of the substructure during deformation [54,69]. Analyzing the results in Figure 14 (d), we can see that the KAM distribution is shifted and slightly wider for Zr(C,N) compared to Ti(C,N). It may appear that the difference is more or less small, however, the KAM was calculated across all the grains in the pillar and also similar differences can be observed for Nickel subjected to increasing strain [54]. Besides, it has been stated that a good correlation between Schmidt factor and KAM values [69] exists. Then looking back at the higher Schmidt factor results, there is a clear indication that the strain has contributed to this higher propensity. We emphasize that the references cited for the gradient formation in the microstructure are for FCC materials deformed during rolling. The latter could be considered as compression in the direction of rolling plane normal [72] which have similarities to our micro-compression test and will induce similar effects.

Calculation of Geometrically Necessary Dislocation (GND) from the misorientation measurements for Zr(C,N) is not precise because of the finer grain size and more importantly to the poor indexing at the grain boundaries.

For the case of Ti(C,N) no gradient is noticed and rather higher misorientations are located at the grain boundaries. As a result, unlike the Zr(C,N) which is deforming as a single structure, Ti(C,N) behaves as discrete arrays of grains sliding to each other and deforming independently. This confirms the earlier discussions for the deformation mechanism of Ti(C,N).

Figure 14:

Summarizing, plastic deformation in ceramics at high temperature is a known fact, and since the 50s and over the past, many studies focused on high temperature plasticity for B1-type structure materials. However, dislocation motion and plasticity at room temperature is rather a recent topic. Kiani et al. [27] proved (using in-situ TEM compression tests) that ZrC monocrystals (which are very similar to Zr(C,N): same B1 lattice, comparable mechanical properties) underwent a plastic deformation at room temperature. They also mentioned that carefully prepared polycrystalline transition metal carbide samples may also undergo plastic deformation at low temperatures upon the fact that multiple slip

systems are active at room temperature [27]. The brittleness of the pillar is related mainly to the polycrystallinity of the pillar and multi-interfaces (due to the micron/sub-micron grain size) that exerts and limits dislocation motion [3]. In literature this phenomenon is introduced as the “microstructural constraint” (coating microstructure here) which is in addition to the “dimensional constraint” (pillar size in our case) that monitor together the dislocation mechanics and hence deformation mechanisms [73–75].

For the brittle failure, the bulk fragile properties take over as a general yielding at the end of the experiment test, which eclipses the local micro-phenomenon occurring at the grain scale. Indeed, the fracture probability of brittle materials decreases for smaller sizes [74] as the miniaturization of the dimension reduces the density of critical defects that causes brittle facture in ceramics. Hence, as the experiment progresses and the probability of a brittle fracture decreases, the internal mechanisms in the grains will take place and plastic deformation can be noticed. Besides, and for an analogy, compression test performed on even bulky (couple of millimeters sized) brittle materials showed that there is a critical size where the deformation switches from brittle to ductile [76]. In other words, having an extended and lasting plastic deformation perceivable in our experiments depend on three things: the intrinsic factors (orientation and grain size), the type and density of grain boundaries and finally the size of the tested sample.

The strong brittleness of Ti(C,N) is mainly attributed to low cohesive strength at the grain boundaries as demonstrated before. Nevertheless, the question about the absence or existence of plasticity within single Ti(C,N) crystals at room temperature cannot be addressed in this investigation. In-situ TEM compression of single crystals would be an effective technique to approach this question. Still, we suggest that the absence or limited dislocation mobility is more intrinsically related. On one side, if we compare the carbides variants (which are comparable to their carbonitrides counterpart), we find that TiC has only one active slip system $\{110\}\langle 1\bar{1}0\rangle$ [14] at low temperatures in contrast to ZrC which has two active slip systems active at room temperature $\{001\}\langle 110\rangle$ and $\{1\bar{1}0\}\langle 110\rangle$ [27]. On the other side, mechanical properties of TMCN are intrinsically related to the electronic structure formed by the ternary compound (Transition Metal, Carbon and Nitrogen), an assumption which was supported earlier by Bilyk [4]. The nature and relative strengths of metal-metal and metal-carbon/nitrogen bonds change with the

valence electron concentration (VEC) in the lattice [19] which makes for example plastic deformation pathways, ductility and hardness vary from TiC to ZrC [27]. Jhi et al. have explained these complex electronic interactions for TiC_xN_{1-x} when nitrogen is replacing carbon in the interstitials sites. They established an evolution of the shear modulus C_{44} with VEC for TiCxN1-x ($0 \leq x \leq 1$), and found that maximum hardness is obtained for VEC = 8.4. Besides, they stated that C_{44} is a good parameter to quantify the resistance of plastic deformation and finally, expected that the same results are to be valid also for other transition metal alloys [19]. Later, Ivashchenko et al. have obtained similar results and explanations for TiC_xN_{1-x} [21] and more interestingly for ZrC_xN_{1-x} as well [22]. Thus, as the same explanation of hardness dependence on the nature of bonding is valid for Ti(C,N) and Zr(C,N), and as C_{44} shear modulus is a good parameter to quantify the resistance of plastic deformation for transition-metal alloys [19], then if we compare the corresponding C_{44} values of each type of coating, we can have a direct idea about the ease of plastic deformation in each case. In doing so, the calculated values are $C_{44}(TiC_{0.5}N_{0.5})$=188 GPa [21], $C_{44}(TiC_{0.5}N_{0.5})$=185 GPa [23] and $C_{44}(ZrC_{0.5}N_{0.5})$=158 GPa [22], and we can see clearly that it is higher for the former. Finally, this means that the brittleness of Ti(C,N) is not only related to low cohesive strength between grains, but also to limited dislocation activation at low temperatures.

4. Conclusions

Throughout different techniques and investigations, the deformation behavior and micro-mechanical properties at room temperature of Ti(C,N) and Zr(C,N) CVD coatings was evaluated. Both Ti(C,N) and Zr(C,N) exhibited high yield strength of 14 GPa. Results revealed that Ti(C,N) undergoes a pure intergranular crack propagation and grain decohesion. Zr(C,N), in addition to its high strength and other outstanding properties, has attested for unexpected plastic deformation at room temperature and formation of strain gradients, as revealed by EBSD analysis. The brittle behavior of Ti(C,N) is dominated by low cohesive strength along the grain boundaries and reduced dislocation activation at low temperatures. Taking into consideration that macroscopic deformation is scaled even on the mesoscale [54], the results presented in this work may explain the enhanced performance of Zr(C,N) under cycling

thermo-mechanical loads by the combination of high hardness, better cohesive strength and its intrinsic plasticity compared to Ti(C,N).

5. Acknowledgements

The authors acknowledge Jeanette Persson (Sandvik Coromant R&D) for producing the CVD coatings, André Tengstrand (Sandvik Coromant R&D) for writing the ANSYS code of FEM analysis, Sebastian Slawik and Sebastián Suárez (Saarland University) for the discussions. The European Commission is acknowledged for funding through the projects: Erasmus Mundus Doctoral Programme DocMASE; RISE Project CREATe-Network (GA N° 644013) and EFRE project AME-Lab (European Regional Development Fund C/4-EFRE-13/2009/Br). Part of this paper was presented at 19th Plansee Seminar 2017, Reutte, Austria.

6. References

[1] C. Mitterer, PVD and CVD Hard Coatings, in: V.K. Sarin, L. Llanes, D. Mari (Eds.), Compr. Hard Mater. - Vol. 2 Ceram., Elsevier, Amsterdam, 2014: pp. 449–468.
[2] J. Garcia, R. Pitonak, The role of cemented carbide functionally graded outer-layers on the wear performance of coated cutting tools, Int. J. Refract. Met. Hard Mater. 36 (2013) 52–59. doi:10.1016/j.ijrmhm.2011.12.007.
[3] Y.X. Wang, S. Zhang, Toward hard yet tough ceramic coatings, Surf. Coat. Technol. 258 (2014) 1–16. doi:10.1016/j.surfcoat.2014.07.007.
[4] I.I. Bilyk, Potentialities of carbonitrides as the hard constituent of sintered hard alloys, Powder Metall. Mater. Parts Coat. 11 (1972) 466–470. doi:10.1007/BF00797922.
[5] W. Lengauer, S. Binder, K. Aigner, P. Ettmayer, A. Guillou, J. Debuigne, G. Groboth, Solid state properties of group IVb carbonitrides, J. Alloys Compd. 217 (1995) 137–147.
[6] Q. Yang, W. Lengauer, T. Koch, M. Scheerer, I. Smid, Hardness and elastic properties of Ti (C x N 1- x), Zr (C x N 1- x) and Hf (C x N 1- x), J. Alloys Compd. 309 (2000) L5–L9.
[7] J. Garcia, M.F. Moreno, J. Östby, J. Persson, H.C. Pinto, Design of coated cemented carbides with improved comb crack resistance, in: Proc. 19th Plansee Semin., Reutte, Austria, 2017.
[8] W.G. Fahrenholtz, G.E. Hilmas, Ultra-high temperature ceramics: Materials for extreme environments, Scr. Mater. 129 (2017) 94–99. doi:10.1016/j.scriptamat.2016.10.018.
[9] W.S. Williams, Influence of Temperature, Strain Rate, Surface Condition, and Composition on the Plasticity of Transition-Metal Carbide Crystals, J. Appl. Phys. 35 (1964) 1329–1338. doi:10.1063/1.1713614.
[10] G.E. Hollox, R.E. Smallman, Plastic Behavior of Titanium Carbide, J. Appl. Phys. 37 (1966) 818–823. doi:10.1063/1.1708264.
[11] D.W. Lee, J.S. Haggerty, Plasticity and creep in single crystals of zirconium carbide, J. Am. Ceram. Soc. 52 (1969) 641–647.

[12] I.V. Gridneva, Y.V. Mil'man, G.A. Rymashevskii, V.I. Trefilov, S.I. Chugunova, Effect of temperature on the strength characteristics of zirconium carbide, Sov. Powder Metall. Met. Ceram. 15 (1976) 638–645. doi:10.1007/BF01159455.
[13] R. Darolia, T.F. Archbold, Plastic deformation of polycrystalline zirconium carbide, J. Mater. Sci. 11 (1976) 283–290.
[14] D.K. Chatterjee, M.G. Mendiratta, H.A. Lipsitt, Deformation behaviour of single crystals of titanium carbide, J. Mater. Sci. 14 (1979) 2151–2156.
[15] E. Breval, Microplasticity at room temperature of single-crystal titanium carbide with different stoichiometry, J. Mater. Sci. 16 (1981) 2781–2788.
[16] G. Das, K.S. Mazdiyasni, H.A. Lipsitt, Mechanical properties of polycrystalline TiC, J. Am. Ceram. Soc. 65 (1982) 104–110.
[17] A.P. Katz, H.A. Lipsitt, T. Mah, M.G. Mendiratta, Mechanical behaviour of polycrystalline TiC, J. Mater. Sci. 18 (1983) 1983–1992.
[18] V.M. SURA, D.L. Kohlstedt, State-Variable Analysis of Inelastic Deformation of TiC Single Crystals, J. Am. Ceram. Soc. 70 (1987) 315–320.
[19] S.-H. Jhi, J. Ihm, S.G. Louie, M.L. Cohen, Electronic mechanism of hardness enhancement in transition-metal carbonitrides, Nature. 399 (1999) 132–134. doi:10.1038/20148.
[20] A. Zaoui, B. Bouhafs, P. Ruterana, First-principles calculations on the electronic structure of TiCxN1−x, ZrxNb1−xC and HfCxN1−x alloys, Mater. Chem. Phys. 91 (2005) 108–115. doi:10.1016/j.matchemphys.2004.10.056.
[21] V.I. Ivashchenko, P.E.A. Turchi, L.A. Ivashchenko, P.L. Skrynskii, Electronic origin of elastic properties of titanium carbonitride alloys, Metall. Mater. Trans. A. 37 (2006) 3391–3396. doi:10.1007/s11661-006-1031-9.
[22] V.I. Ivashchenko, P.E.A. Turchi, V.I. Shevchenko, First-principles study of elastic and stability properties of ZrC–ZrN and ZrC–TiC alloys, J. Phys. Condens. Matter. 21 (2009) 395503. doi:10.1088/0953-8984/21/39/395503.
[23] W. Feng, S. Cui, H. Hu, G. Zhang, Z. Lv, Electronic structure and elastic constants of TiCxN1−x, ZrxNb1−xC and HfCxN1−x alloys: A first-principles study, Phys. B Condens. Matter. 406 (2011) 3631–3635. doi:10.1016/j.physb.2011.06.058.
[24] R.F. Zhang, S.H. Sheng, S. Veprek, Origin of different plastic resistance of transition metal nitrides and carbides: Stiffer yet softer, Scr. Mater. 68 (2013) 913–916. doi:10.1016/j.scriptamat.2013.01.040.
[25] S.K. Yadav, R. Ramprasad, A. Misra, X.-Y. Liu, Core structure and Peierls stress of edge and screw dislocations in TiN: A density functional theory study, Acta Mater. 74 (2014) 268–277. doi:10.1016/j.actamat.2014.04.047.
[26] V. Krasnenko, M.G. Brik, First-principles calculations of the structural, elastic and electronic properties of MNxC1−x (M = Ti, Zr, Hf; 0 ≤ x ≤ 1) carbonitrides at ambient and elevated hydrostatic pressure, Solid State Sci. 28 (2014) 1–8. doi:10.1016/j.solidstatesciences.2013.11.012.
[27] S. Kiani, C. Ratsch, A.M. Minor, S. Kodambaka, J.-M. Yang, Orientation- and size-dependent room-temperature plasticity in ZrC crystals, Philos. Mag. 95 (2015) 985–997. doi:10.1080/14786435.2015.1012568.
[28] T. Li, T. Liu, L. Zhang, T. Fu, H. Wei, First-principles investigation on slip systems and twinnability of TiC, Comput. Mater. Sci. 126 (2017) 103–107. doi:10.1016/j.commatsci.2016.09.028.
[29] J. Kim, Y.J. Suh, Temperature- and pressure-dependent elastic properties, thermal expansion ratios, and minimum thermal conductivities of ZrC, ZrN, and Zr(C 0.5 N 0.5), Ceram. Int. 43 (2017) 12968–12974. doi:10.1016/j.ceramint.2017.06.195.
[30] G. Dehm, H.P. Wörgötter, S. Cazottes, J.M. Purswani, D. Gall, C. Mitterer, D. Kiener, Can micro-compression testing provide stress–strain data for thin films?, Thin Solid Films. 518 (2009) 1517–1521. doi:10.1016/j.tsf.2009.09.070.
[31] T.-H. Fang, S.-R. Jian, D.-S. Chuu, Nanomechanical properties of TiC, TiN and TiCN thin films using scanning probe microscopy and nanoindentation, Appl. Surf. Sci. 228 (2004) 365–372. doi:10.1016/j.apsusc.2004.01.053.
[32] S. Bhowmick, R. Bhide, M. Hoffman, V. Jayaram *, S.K. Biswas, Fracture mode transitions during indentation of columnar TiN coatings on metal, Philos. Mag. 85 (2005) 2927–2945. doi:10.1080/14786430500155213.
[33] M.T. Tilbrook, D.J. Paton, Z. Xie, M. Hoffman, Microstructural effects on indentation failure mechanisms in TiN coatings: Finite element simulations, Acta Mater. 55 (2007) 2489–2501. doi:10.1016/j.actamat.2006.11.043.

[34] Z.H. Xie, M. Hoffman, P. Munroe, A. Bendavid, P.J. Martin, Deformation mechanisms of TiN multilayer coatings alternated by ductile or stiff interlayers, Acta Mater. 56 (2008) 852–861. doi:10.1016/j.actamat.2007.10.047.
[35] Y. Sun, C. Lu, H. Yu, A. Kiet Tieu, L. Su, Y. Zhao, H. Zhu, C. Kong, Nanomechanical properties of TiCN and TiCN/Ti coatings on Ti prepared by Filtered Arc Deposition, Mater. Sci. Eng. A. 625 (2015) 56–64. doi:10.1016/j.msea.2014.11.093.
[36] A. Zeilinger, J. Todt, C. Krywka, M. Müller, W. Ecker, B. Sartory, M. Meindlhumer, M. Stefenelli, R. Daniel, C. Mitterer, J. Keckes, In-situ Observation of Cross-Sectional Microstructural Changes and Stress Distributions in Fracturing TiN Thin Film during Nanoindentation, Sci. Rep. 6 (2016). doi:10.1038/srep22670.
[37] R. Warren, Measurement of the fracture properties of brittle solids by Hertzian indentation, Acta Metall. 26 (1978) 1759–1769.
[38] H. Pelletier, J. Krier, A. Cornet, P. Mille, Limits of using bilinear stress–strain curve for finite element modeling of nanoindentation response on bulk materials, Thin Solid Films. 379 (2000) 147–155.
[39] J.J. Gilman, Chemistry and physics of mechanical hardness, Wiley, Hoboken, N.J, 2009.
[40] D. Kiener, C. Motz, G. Dehm, Micro-compression testing: A critical discussion of experimental constraints, Mater. Sci. Eng. A. 505 (2009) 79–87. doi:10.1016/j.msea.2009.01.005.
[41] H. Fei, A. Abraham, N. Chawla, H. Jiang, Evaluation of micro-pillar compression tests for accurate determination of elastic-plastic constitutive relations, J. Appl. Mech. 79 (2012) 061011.
[42] S. Korte, J.S. Barnard, R.J. Stearn, W.J. Clegg, Deformation of silicon – Insights from microcompression testing at 25–500℃, Int. J. Plast . 27 (2011) 1853–1866. doi:10.1016/j.ijplas.2011.05.009.
[43] N. Kheradmand, H. Vehoff, A. Barnoush, An insight into the role of the grain boundary in plastic deformation by means of a bicrystalline pillar compression test and atomistic simulation, Acta Mater. 61 (2013) 7454–7465. doi:10.1016/j.actamat.2013.08.056.
[44] S. Korte-Kerzel, Microcompression of brittle and anisotropic crystals: recent advances and current challenges in studying plasticity in hard materials, MRS Commun. 7 (2017) 109–120. doi:10.1557/mrc.2017.15.
[45] Y. Zou, H. Ma, R. Spolenak, Ultrastrong ductile and stable high-entropy alloys at small scales, Nat. Commun. 6 (2015) 7748. doi:10.1038/ncomms8748.
[46] J.M. Wheeler, R. Raghavan, V. Chawla, M. Morstein, J. Michler, Deformation of Hard Coatings at Elevated Temperatures, Surf. Coat. Technol. 254 (2014) 382–387. doi:10.1016/j.surfcoat.2014.06.048.
[47] S. Liu, R. Raghavan, X.T. Zeng, J. Michler, W.J. Clegg, Compressive deformation and failure of CrAlN/Si3N4 nanocomposite coatings, Appl. Phys. Lett. 104 (2014) 081919.
[48] S. Liu, J.M. Wheeler, J. Michler, X.T. Zeng, W.J. Clegg, Plastic flow at the theoretical yield stress in ceramic films, Scr. Mater. 117 (2016) 24–27. doi:10.1016/j.scriptamat.2016.02.008.
[49] M. Schlögl, C. Kirchlechner, J. Paulitsch, J. Keckes, P.H. Mayrhofer, Effects of structure and interfaces on fracture toughness of CrN/AlN multilayer coatings, Scr. Mater. 68 (2013) 917–920. doi:10.1016/j.scriptamat.2013.01.039.
[50] Y. Mu, X. Zhang, J.W. Hutchinson, W.J. Meng, Measuring critical stress for shear failure of interfacial regions in coating/interlayer/substrate systems through a micro-pillar testing protocol, J. Mater. Res. 32 (2017) 1421–1431. doi:10.1557/jmr.2016.516.
[51] H. Zhang, B.E. Schuster, Q. Wei, K.T. Ramesh, The design of accurate micro-compression experiments, Scr. Mater. 54 (2006) 181–186. doi:10.1016/j.scriptamat.2005.06.043.
[52] D.P. Field, K.R. Magid, I.N. Mastorakos, J.N. Florando, D.H. Lassila, J.W. Morris, Mesoscale strain measurement in deformed crystals: A comparison of X-ray microdiffraction with electron backscatter diffraction, Philos. Mag. 90 (2010) 1451–1464. doi:10.1080/14786430903397297.
[53] J.-J. Fundenberger, A. Morawiec, E. Bouzy, J.S. Lecomte, Polycrystal orientation maps from TEM, Ultramicroscopy. 96 (2003) 127–137. doi:10.1016/S0304-3991(02)00435-7.
[54] N.P. Gurao, S. Suwas, Generalized scaling of misorientation angle distributions at meso-scale in deformed materials, Sci. Rep. 4 (2015). doi:10.1038/srep05641.
[55] T. Csanádi, P. Szommer, N.Q. Chinh, S. Grasso, J. Dusza, M. Reece, Plasticity in ZrB 2 micropillars induced by anomalous slip activation, J. Eur. Ceram. Soc. 36 (2016) 389–394. doi:10.1016/j.jeurceramsoc.2015.10.035.
[56] J.M. Wheeler, C. Niederberger, C. Tessarek, S. Christiansen, J. Michler, Extraction of plasticity parameters of GaN with high temperature, in situ micro-compression, Int. J. Plast. 40 (2013) 140–151. doi:10.1016/j.ijplas.2012.08.001.

[57] T. Csanádi, M. Bľanda, A. Duszová, N.Q. Chinh, P. Szommer, J. Dusza, Deformation characteristics of WC micropillars, J. Eur. Ceram. Soc. 34 (2014) 4099–4103. doi:10.1016/j.jeurceramsoc.2014.05.045.
[58] J.M. Tarragó, J.J. Roa, E. Jiménez-Piqué, E. Keown, J. Fair, L. Llanes, Mechanical deformation of WC–Co composite micropillars under uniaxial compression, Int. J. Refract. Met. Hard Mater. 54 (2016) 70–74. doi:10.1016/j.ijrmhm.2015.07.015.
[59] J.P. Best, J. Wehrs, X. Maeder, J. Zechner, J.M. Wheeler, T. Schär, M. Morstein, J. Michler, Reversible, high temperature softening of plasma-nitrided hot-working steel studied using in situ micro-pillar compression, Mater. Sci. Eng. A. 680 (2017) 433–436. doi:10.1016/j.msea.2016.11.003.
[60] O.N. Senkov, G.B. Wilks, J.M. Scott, D.B. Miracle, Mechanical properties of Nb25Mo25Ta25W25 and V20Nb20Mo20Ta20W20 refractory high entropy alloys, Intermetallics. 19 (2011) 698–706. doi:10.1016/j.intermet.2011.01.004.
[61] Y. Zou, S. Maiti, W. Steurer, R. Spolenak, Size-dependent plasticity in an Nb25Mo25Ta25W25 refractory high-entropy alloy, Acta Mater. 65 (2014) 85–97. doi:10.1016/j.actamat.2013.11.049.
[62] S.I. Wright, M.M. Nowell, D.P. Field, A Review of Strain Analysis Using Electron Backscatter Diffraction, Microsc. Microanal. 17 (2011) 316–329. doi:10.1017/S1431927611000055.
[63] D.A. Hughes, Q. Liu, D.C. Chrzan, N. Hansen, Scaling of microstructural parameters: misorientations of deformation induced boundaries, Acta Mater. 45 (1997) 105–112.
[64] D.A. Hughes, D.C. Chrzan, Q. Liu, N. Hansen, Scaling of misorientation angle distributions, Phys. Rev. Lett. 81 (1998) 4664.
[65] Q. Liu, N. Hansen, Geometrically necessary boundaries and incidental dislocation boundaries formed during cold deformation, Scr. Metall. Mater. 32 (1995) 1289–1295.
[66] A.M. Korsunsky, M. Sebastiani, E. Bemporad, Focused ion beam ring drilling for residual stress evaluation, Mater. Lett. 63 (2009) 1961–1963. doi:10.1016/j.matlet.2009.06.020.
[67] M. Sebastiani, C. Eberl, E. Bemporad, G.M. Pharr, Depth-resolved residual stress analysis of thin coatings by a new FIB–DIC method, Mater. Sci. Eng. A. 528 (2011) 7901–7908. doi:10.1016/j.msea.2011.07.001.
[68] L. Clément, R. Pantel, L.F.T. Kwakman, J.L. Rouvière, Strain measurements by convergent-beam electron diffraction: The importance of stress relaxation in lamella preparations, Appl. Phys. Lett. 85 (2004) 651–653. doi:10.1063/1.1774275.
[69] N.P. Gurao, S. Suwas, Deformation behaviour at macro- and nano-length scales: The development of orientation gradients, Mater. Lett. 99 (2013) 81–85. doi:10.1016/j.matlet.2013.02.074.
[70] R.W. Harrison, W.E. Lee, Processing and properties of ZrC, ZrN and ZrCN ceramics: a review, Adv. Appl. Ceram. 115 (2016) 294–307. doi:10.1179/1743676115Y.0000000061.
[71] L. Toth, Mechanical Properties, in: Transit. Met. Carbides Nitrides, 1st ed., Academic Press, 1971: p. 279.
[72] R.. Smallman, D. Green, The dependence of rolling texture on stacking fault energy, Acta Metall. 12 (1964) 145–154. doi:10.1016/0001-6160(64)90182-8.
[73] R.W. Armstrong, On size effects in polycrystal plasticity, J. Mech. Phys. Solids. 9 (1961) 196–199. doi:10.1016/0022-5096(61)90018-7.
[74] E. Arzt, Size effects in materials due to microstructural and dimensional constraints: a comparative review, Acta Mater. 46 (1998) 5611–5626.
[75] J.R. Greer, J.T.M. De Hosson, Plasticity in small-sized metallic systems: Intrinsic versus extrinsic size effect, Prog. Mater. Sci. 56 (2011) 654–724. doi:10.1016/j.pmatsci.2011.01.005.
[76] K. Kendall, Complexities of compression failure, in: Proc. R. Soc. Lond. Math. Phys. Eng. Sci., The Royal Society, 1978: pp. 245–263.

TABLES

Table 1: Mechanical properties of different materials (* [19]; ** Sandvik Coromant database) .

Material	Young´s modulus E (GPa)	Shear modulus G (GPa)
$Zr(C_{0,5},N_{0,5})$*	405	172
$Ti(C_{0,5},N_{0,5})$*	463	194
TiN*	465	189
WC-Co**	626	257

FIGURES

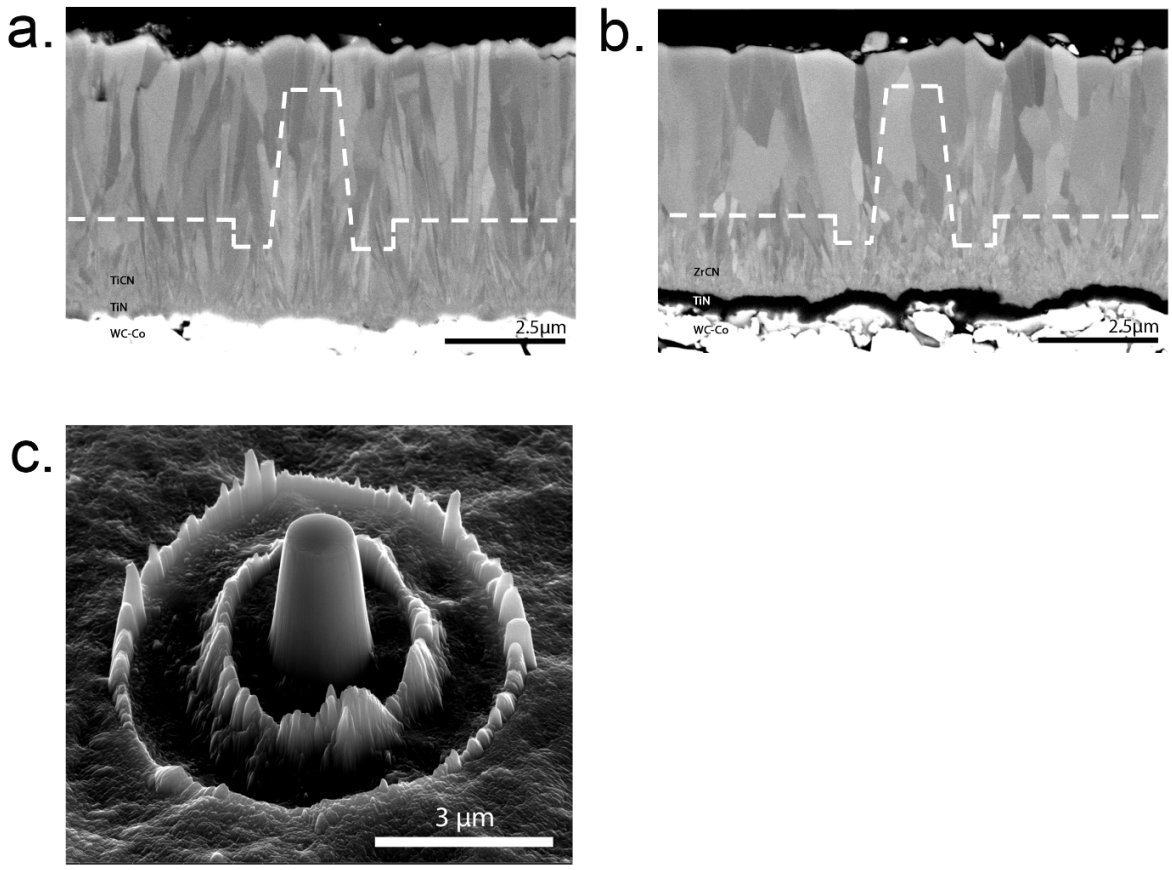

Figure 1: (a) Cross section image (SEM) of Zr(C,N) and (b) Ti(C,N) coatings investigated. Surface topography can be seen at the edge. White dashed line indicates the position where pillars were milled. (c) Final pillar shape milled from Ti(C,N) coating.

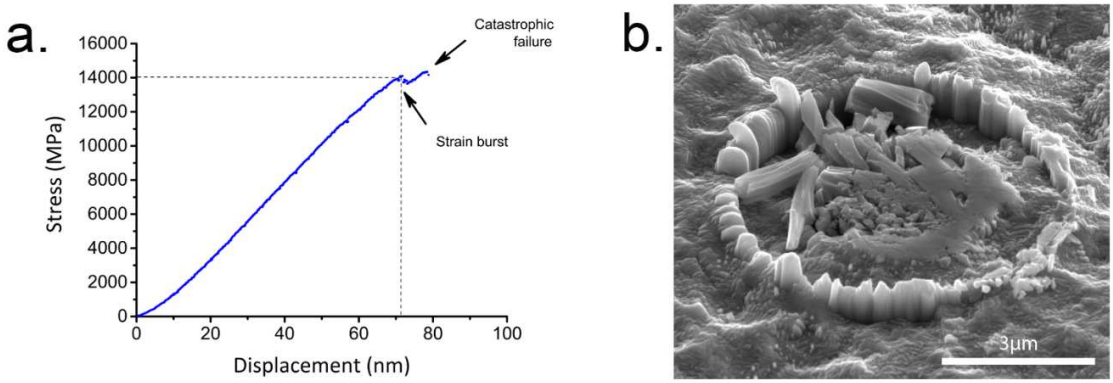

Figure 2: (a) Stress-displacement of a Ti(C,N) pillar (b) Destroyed Ti(C,N) pillar after completion of the loading function.

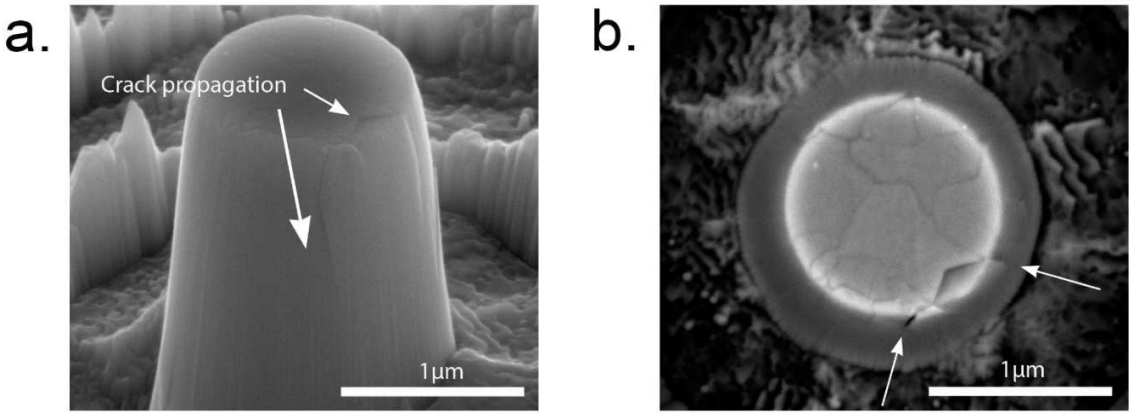

Figure 3: (a) Cracks (white arrows) at the sides of Ti(C,N) pillar following intergranular path which can be seen in the corresponding top view in (b).

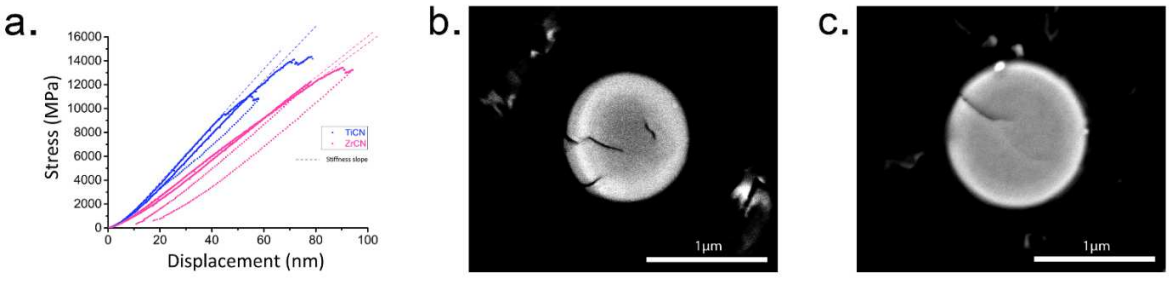

Figure 4: (a) Stress-displacement for selected Ti(C,N) and Zr(C,N) pillars, the stiffness slope is extended. (b), (c) Top view of two

Zr(C,N) pillars after compression. The crack propagation mode seems to be a mixed inter/intragranular mode.

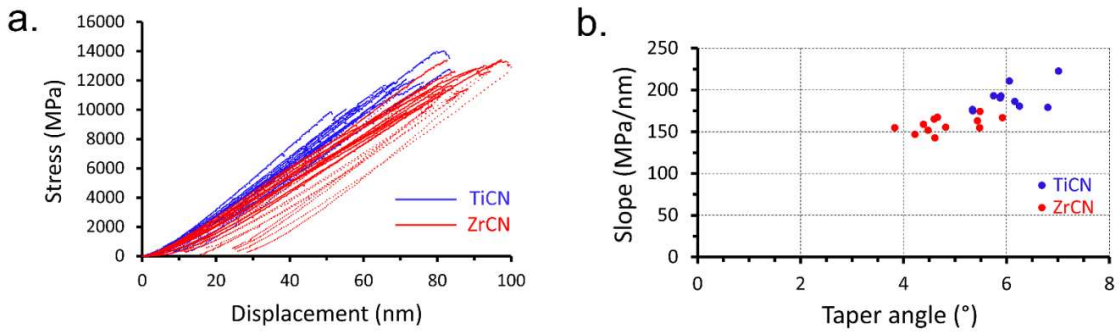

Figure 5: (a) Recap of all stress-displacement curves. (b) Slope of stress-displacement curve vs tapering angle.

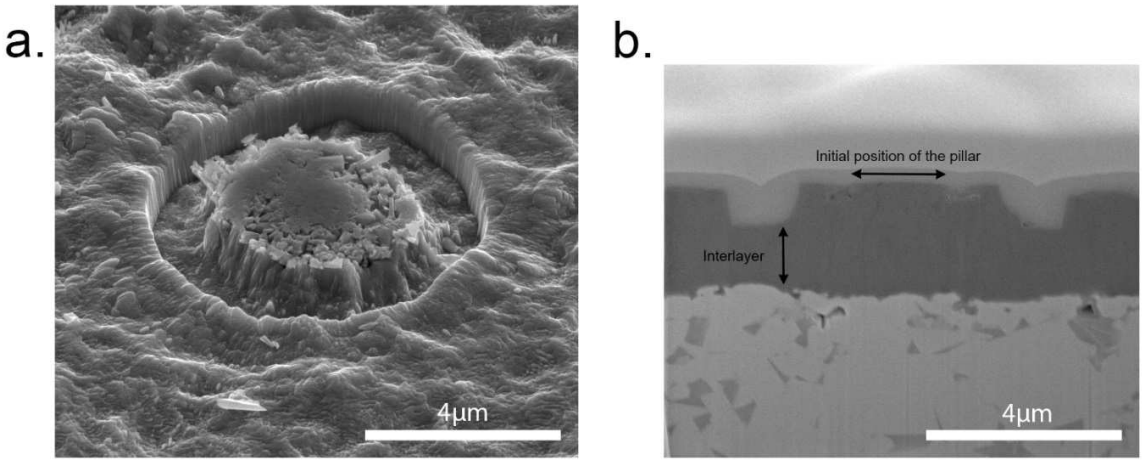

Figure 6: (a) Destroyed Ti(C,N) pillar after compression. (b) Corresponding FIB cross section showing no damage in the supporting interlayer.

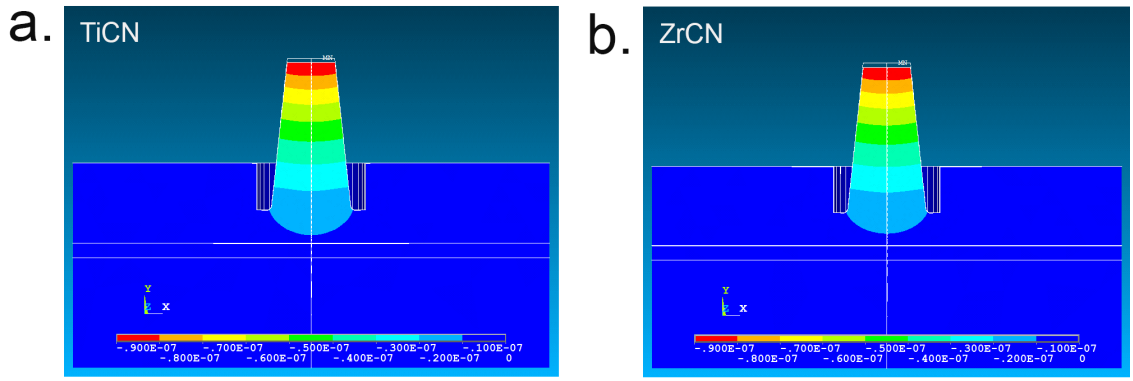

Figure 7: FEM model of Uy displacement (m^{-1}) at 90 nm penetration depth for Ti(C,N) (a) and for Zr(C,N) (b).

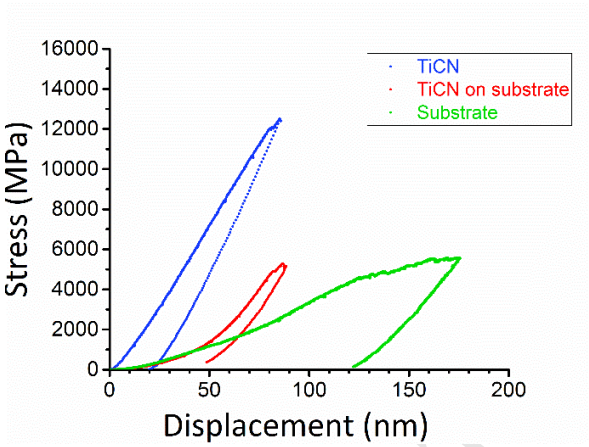

Figure 8: Comparison of deformation between three assemblies: Normal experimental Ti(C,N) pillar (blue curve), Ti(C,N) pillar settling directly on a substrate (red curve) and a pillar carved from a substrate.

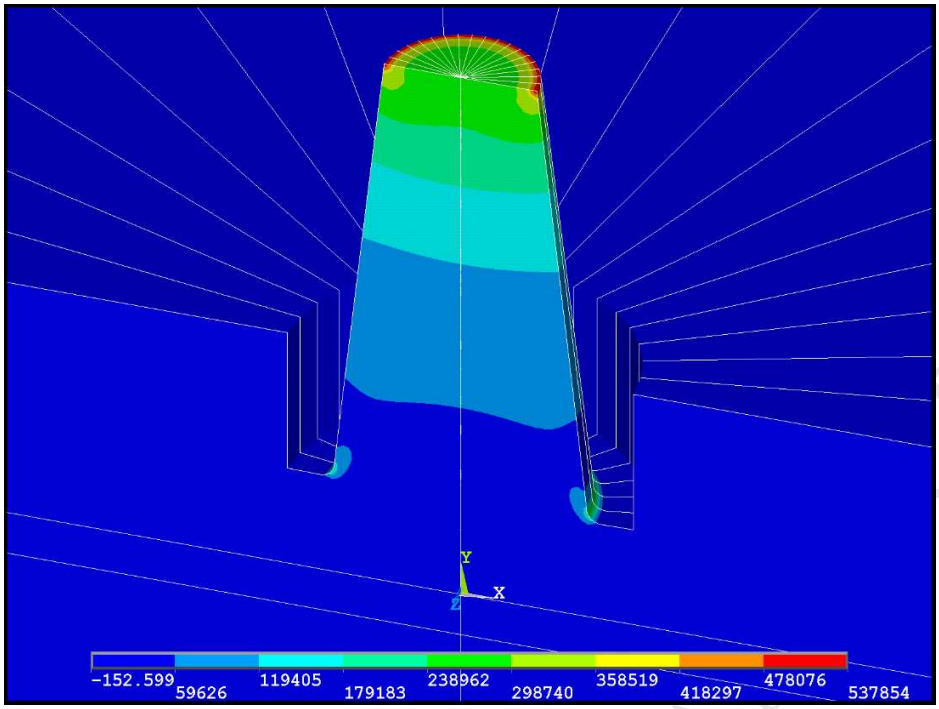

Figure 9: FEM model of strain energy density (J/m^3) at 90 nm penetration depth. The energy density is maximum at the circumference of the pillar's apex region.

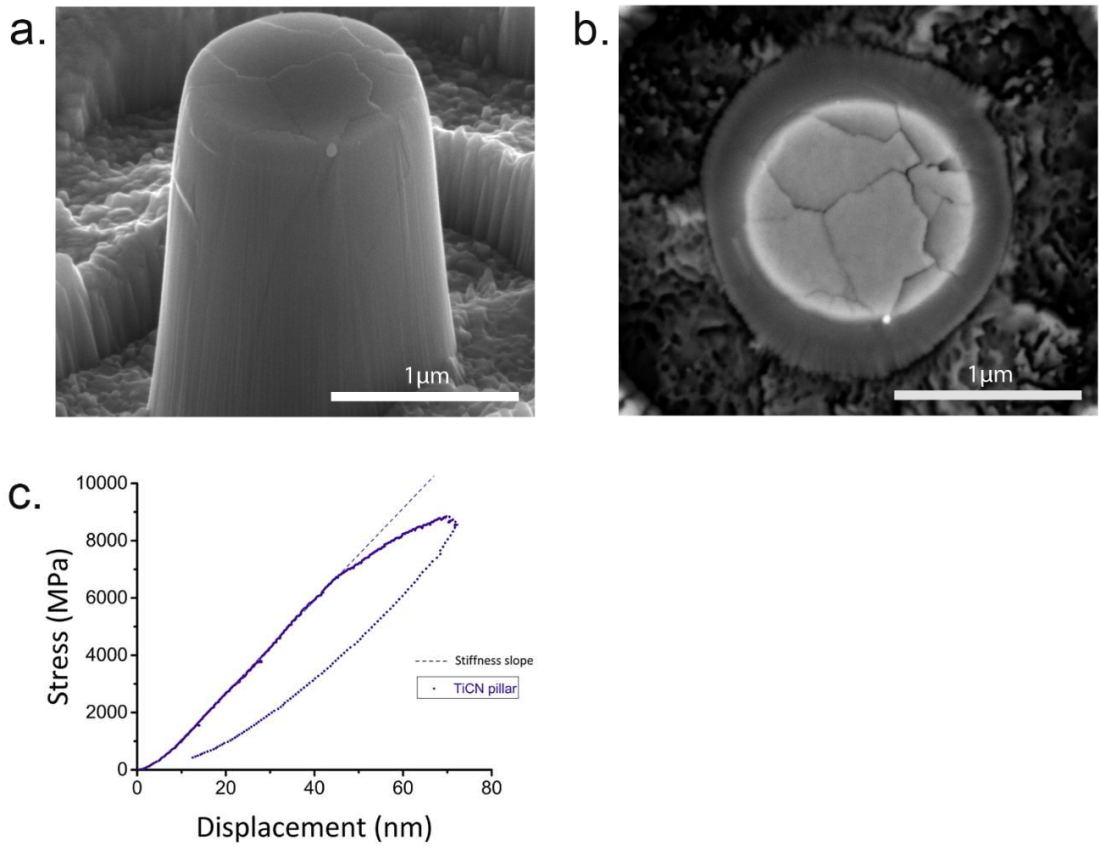

Figure 10: (a) Topography steps on the top surface of the pillar indicating independent elastic recovery for each single grain. (b) Associated top-view showing decohesion of the grains and cracks following intergranular patterns. (c) Corresponding stress-displacement curve showing non-linear behavior due to grain sliding.

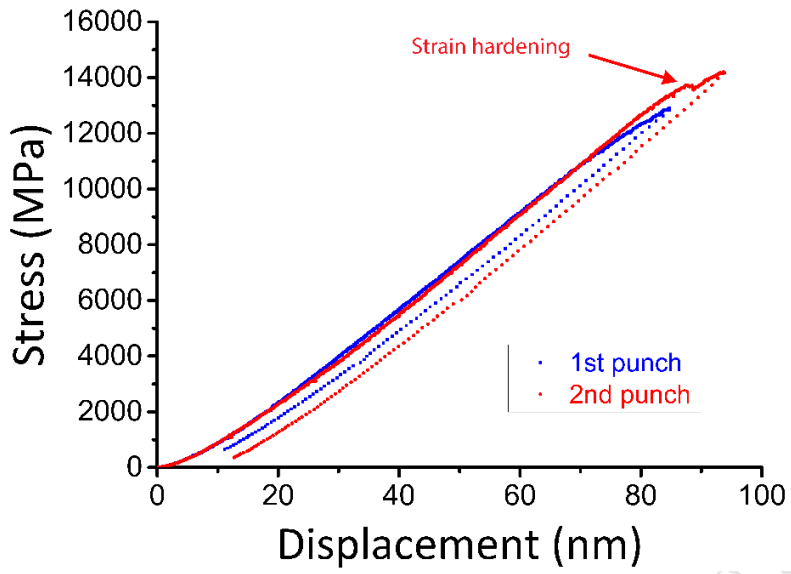

Figure 11: Comparison between two successive compression tests for a Zr(C,N) pillar. Strain hardening is perceived during the 2nd punch.

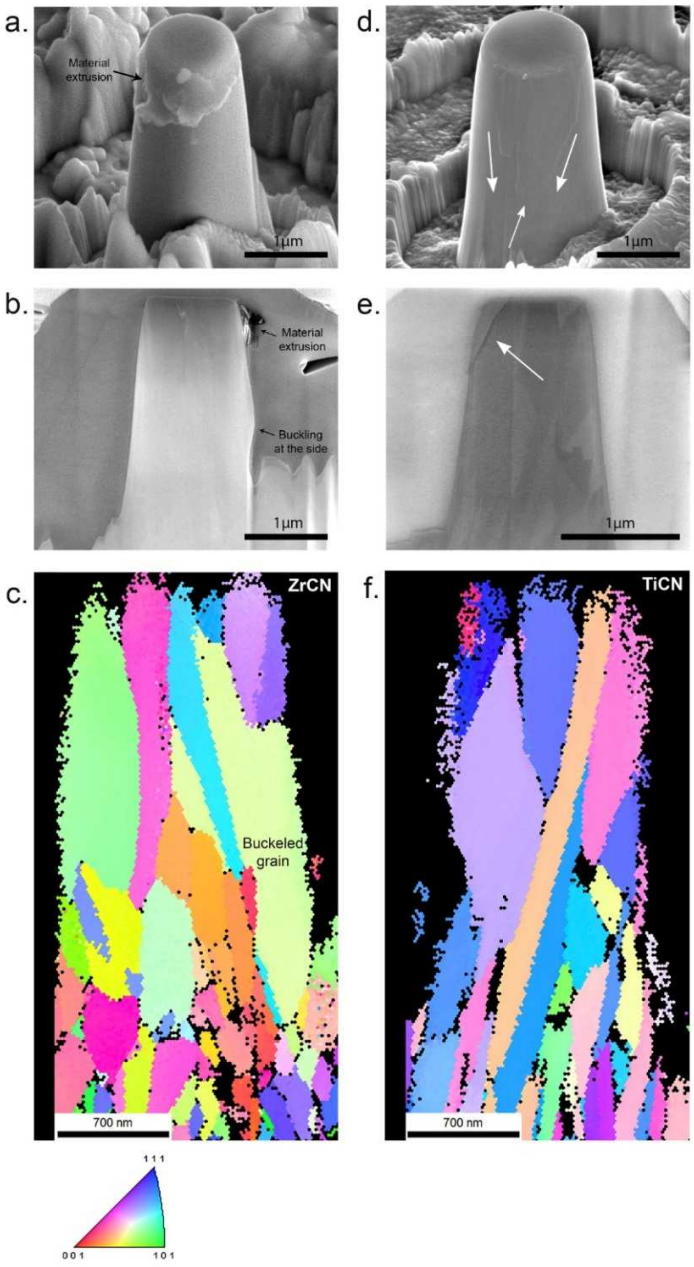

Figure 12: Comparison of yielding events between Zr(C,N) (a-c) and Ti(C,N) (d-f). (a) Yielding at the top side part of a Zr(C,N) pillar. (b) Corresponding FIB cross section according to the vertical axis at the middle. (c) Corresponding Pole Figure map along the vertical axis. (d) Grain slide at the side of a Ti(C,N) pillar. (e) Corresponding FIB cross section according to the vertical axis at the middle. (f) Corresponding Pole Figure map along the vertical axis.

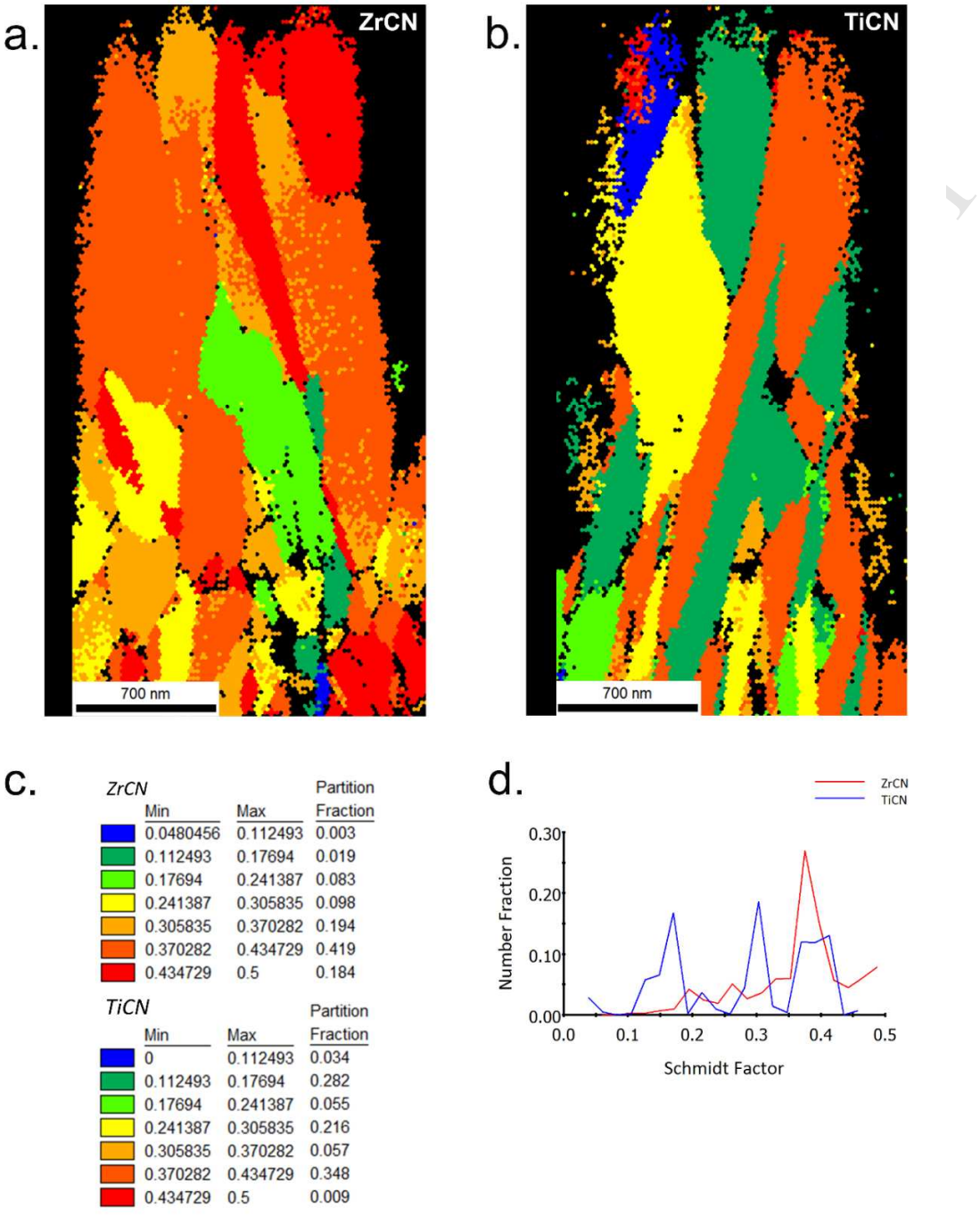

Figure 13: Schmidt factor map for Zr(C,N) (a) and Ti(C,N) (b) (Map legend in (c)). (d) Schmidt factor distribution in Zr(C,N) and Ti(C,N).

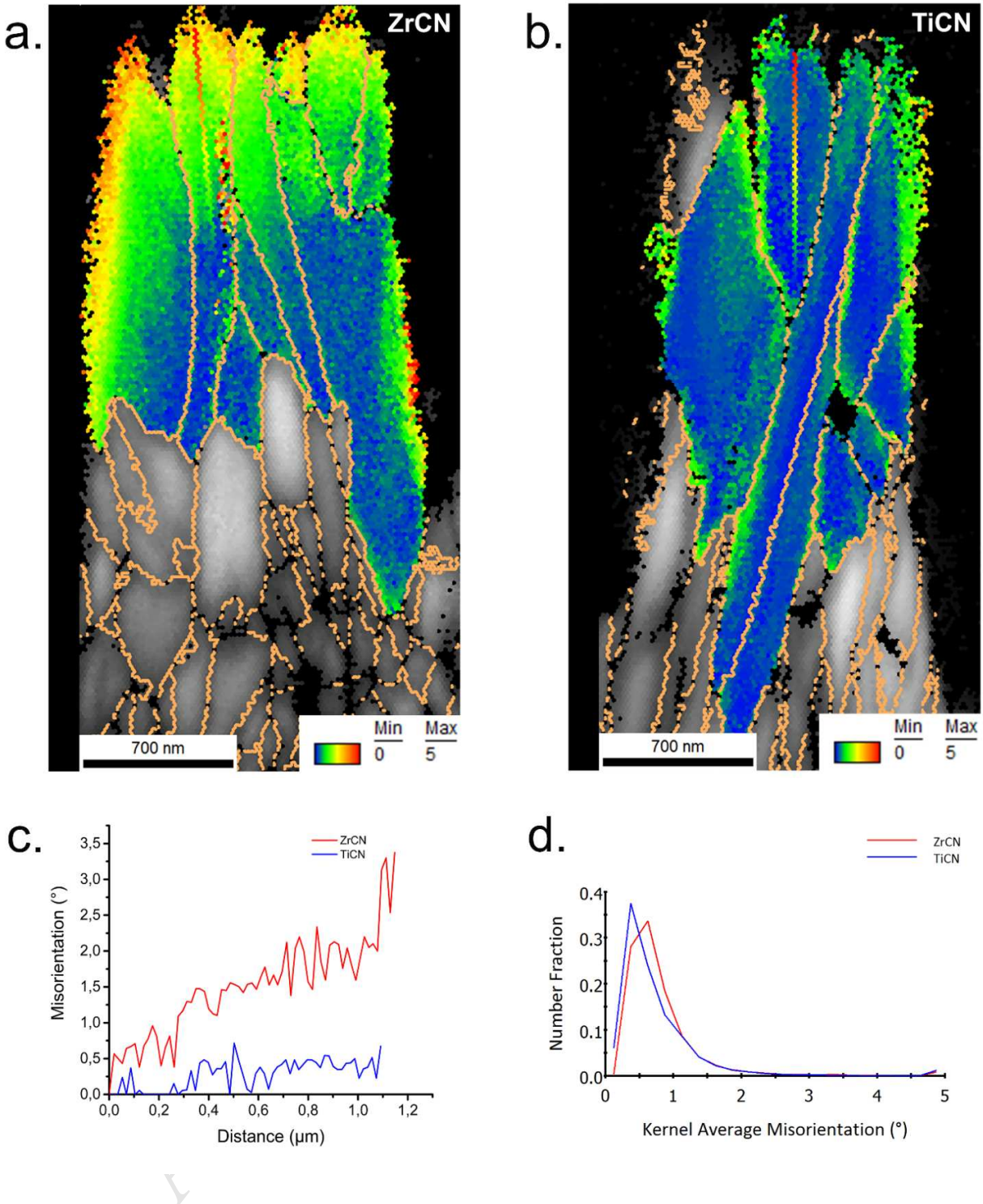

Figure 14: Misorientation analysis with respect to a reference point for (a) Zr(C,N) (b) Ti(C,N). (c) Misorientation profile according to the drawn line (a) and (b). (d) Kernel Average Misorientation (KAM) of Zr(C,N) vs Ti(C,N) calculated across the entire pillar.